Journal of
Materials Chemistry A

ROYAL SOCIETY
OF CHEMISTRY

PAPER

View Article Online
View Journal

Check for updates

Cite this: DOI: 10.1039/d6ta00347h

Loosely packed catalyst layers promote gas transport and flooding resistance in gas diffusion electrodes for electrochemical CO_2 reduction

Thi Ha My Pham,*[ab] Jie Zhang,[c] Loris Lombardo[abd] and Andreas Züttel[ab]

Received 13th January 2026
Accepted 27th March 2026

DOI: 10.1039/d6ta00347h

rsc.li/materials-a

Acidic CO_2 electrolysis enables high CO_2 utilization through carbonate protonation and high C_{2+} selectivity due to the elevated local alkalinity, yet its lifetime remains limited by gas diffusion electrode flooding. In this study, we reveal that a loosely packed, house-of-cards structure can be obtained by incorporating 2D-structured graphene nanoplatelets (GNPs) with Cu-based catalysts, effectively mitigating flooding. With an optimal GNP content below 9 wt%, this structure enhances CO_2 diffusion and significantly improves electrode lifetime, reaching 10 hours at a high current density of 600 mA cm^{-2}. Excessive GNP content leads to catalyst layer densification and accelerates flooding, highlighting the importance of a structure sufficiently thick to accommodate liquid seepage but also sufficiently porous to allow CO_2 access throughout the entire thickness. Our findings provide insights into a practical microstructural strategy for developing efficient and stable CO_2 electrolysis systems.

Introduction

The electrochemical carbon dioxide reduction reaction (eCO_2RR) – occurring at room temperature and ambient pressure and involving the direct use of electricity – represents a promising strategy for mitigating CO_2 emissions.[1,2] This reaction between CO_2 and water shows potential for the storage of renewable energy in the form of valuable chemical feedstocks, such as hydrocarbons.[3,4] The reaction activity and product selectivity depend on the choice of catalysts and the reaction conditions[5,6] and can be regulated *via*, for example, catalyst development, designing/tailoring the interfacial environment, and systems engineering. In the eCO_2RR, the local microenvironment around the catalyst has a significant effect on the faradaic efficiency (FE) towards CO_2RR products relative to the competing hydrogen evolution reaction (HER). Due to the limited solubility of CO_2 in water, the eCO_2RR is typically conducted at a neutral pH, ensuring a balance that minimises the HER (favoured by an excess of protons) while also avoiding the formation of carbonate species (which occurs under conditions of excess OH^-).[7]

Flow cell reactors, in which CO_2 is fed from the rear of a gas diffusion electrode (GDE), effectively address the challenge of the limited solubility of CO_2 in aqueous electrolytes.[8] Catalysts are typically drop-cast, spray-coated, or directly grown on a hydrophobic microporous layer (MPL), which sits atop a gas diffusion layer (GDL) composed of carbon cloth. The CO_2, introduced from the rear of the GDE, diffuses first through the GDL and subsequently through the MPL before reaching the catalyst layer (CL). This rear-fed configuration reduces the diffusion distance of CO_2 in the liquid phase (on the order of micrometres), thereby enhancing the local CO_2 concentration near the catalyst surface compared to H-cell setups. Flow cells can thus operate at current densities of hundreds of mA cm^{-2}, significantly higher than the tens of mA cm^{-2} typically achievable in H-cells.

Nevertheless, while a flow cell enables operation at high current densities, it often faces a trade-off in terms of a limited operational timeline due to various degradation mechanisms, such as flooding, species evolution in the catholyte and anolyte, membrane degradation, and catalyst reconstruction.[9] Among these, flooding is one of the most critical issues, limiting the operational time to only several hours.[9,10] Under a high current density, the potential-driven off-equilibrium conditions often cause the electrolyte to penetrate the MPL, which can then lead to salt crystallisation (upon reaching the solubility limit) due to water evaporation.[11] These salt crystals typically accumulate in the MPL, blocking CO_2 access to the CL. Once flooding begins, the reduced CO_2 diffusion to the catalyst is reflected in a decrease in the CO_2RR selectivity and an increase in the HER.[12] From the onset of flooding to its progression to severe flooding, salt crystals progressively spread within the GDL, not only blocking CO_2 access to the catalyst but also preventing the gas products from leaving the reaction site, indicating the complete degradation of the GDE.

---

[a] Laboratory of Materials for Renewable Energy (LMER), Institute of Chemical Sciences and Engineering (ISIC), Basic Science Faculty (SB), Ecole Polytechnique Fédérale de Lausanne (EPFL) Valais/Wallis, Energypolis, Rue de l'Industrie 17, CH-1951 Sion, Switzerland. E-mail: thi.pham@epfl.ch

[b] EMPA Materials & Technology, CH-8600 Dübendorf, Switzerland

[c] Key Laboratory of Quantitative Synthetic Biology, Shenzhen Institute of Synthetic Biology, Shenzhen Institute of Advanced Technology, Chinese Academy of Sciences, Shenzhen 518055, China. E-mail: j.zhang5@siat.ac.cn

[d] Institute for Materials Research, Tohoku University, Sendai, Miyagi 980-8577, Japan

Strategies for modifying the GDE to improve its resistance to flooding include GDL, MPL, and CL engineering.[10,13–15] A common approach for all three components is tuning their wettability by adding hydrophobic materials or ionomers to their structures.[11,16] The wetproofing of the GDL can be adjusted to achieve optimal CO_2RR selectivity *versus* the HER; for example, 10% wetproofing allows for maximal CO FE on an Ag catalyst, as it provides the ideal balance between hydrophobicity and electrical conductivity.[17] The resistance to flooding can also be improved by incorporating a PTFE/carbon black layer between the GDL and MPL *via* vacuum-assisted infiltration.[18] The hydrophobicity of the CL is usually improved by mixing the catalyst with hydrophobic binders (*e.g.*, PTFE or PDMS),[19–21] fluorinated silane, or hydrophobic ionomers such as PFSA.[8,22] Compared to the MPL, which serves as a potentially highly hydrophobic barrier to repel water and enable CO_2 flow, the CL must ensure adequate ionic conductivity and water activity while avoiding full flooding to maintain sufficient CO_2 access. Often, increasing the hydrophobicity comes at the expense of electrical conductivity and the electrochemical surface area; thus, the type and amount of the hydrophobic additive must be optimised.[23] While insufficient hydrophobicity can lead to the complete flooding of the metal-based CL and long CO_2 diffusion pathways, an excessive quantity of hydrophobic material, combined with capillary forces, requires a high capillary pressure to wet the CL, resulting in only the partial hydration of the catalyst. Therefore, the catalysts should ideally be covered with a thin layer of electrolyte without the full flooding of the pores, which might be achieved with larger hydrophobic pores.[24] While some studies have focused on bridging the gap in the hydrophobicity between the MPL and CL by tuning the MPL through, for example, the creation of a hydrophobicity gradient zone within the MPL,[25,26] research efforts on designing the CL itself, to the best of our knowledge, are limited. A notable approach to increasing the pore size is the incorporation of two-dimensional (2D) structures, such as nanosheets derived from exfoliated layered double hydroxides, which can assemble into a house-of-cards architecture to enhance pore connectivity and create larger voids.[27] However, the primary focus of such works has been to enable catalyst loadings as high as 5.82 mg cm^{-2} by improving gas and electrolyte transport.

Herein, we employ the house-of-cards structural design to create larger pores within the CL, enhancing CO_2 diffusion through it. By combining a high-void-fraction architecture with a thin hydrophobic binder layer, the CL maintains an optimal "wet-but-not-flooded" state, thereby extending the gas–liquid interaction zone. In this configuration, the selectivity towards C_{2+} products reaches 70% in the acidic reaction environment due to the high local alkalinity at the catalytic sites, while the house-of-cards scaffold improves the resistance to flooding and increases the operational lifetime of the GDE from 2 to 10 hours.

Results and discussion

Acidic CO_2RR over highly porous CuO catalysts

The Cu-based catalyst herein, synthesised using a similar protocol to previous works, involves Cu(II) oxide,[19,28] showcasing a highly porous network morphology (Fig. 1a). The catalyst primarily comprises nanoparticles assembled into high-aspect-ratio needles that are 200 to 500 nm long and 15 to 30 nm wide (Fig. 1a, b and S1). High-resolution transmission electron microscopy (HR-TEM) images, along with the corresponding fast Fourier transform (FFT) patterns and their rotational average intensity, indicate a polycrystalline copper oxide structure, with diffraction peaks matching those of PDF 04-007-0518 (Fig. 1c). In our prior work, this catalyst demonstrated >25% selectivity towards H_2 in 0.1 M $KHCO_3$ within an H-cell. Considering these results, we hypothesised that using an acidic electrolyte would yield a higher FE for H_2.[19] Consequently, CO_2 electrolysis was exclusively conducted under acidic conditions in a flow cell. A single-pass configuration was used to mitigate OH^- and liquid product recirculation, as previously demonstrated.[29]

At a current density of 600 mA cm^{-2}, the CO_2RR product distribution on CuO across three acidic pH conditions (3 M KCl adjusted to pH 1, 2, and 3 with H_3PO_4) and in an alkaline environment (1 M KOH, pH 14) was compared. The FE for H_2 remains approximately 10% under all acidic conditions, while the CO_2RR products account for around 90%, demonstrating the effective suppression of H_2 evolution in acidic electrolytes by the added K^+ ions (Fig. 1d).[22,30,31] Across all acidic pH values,

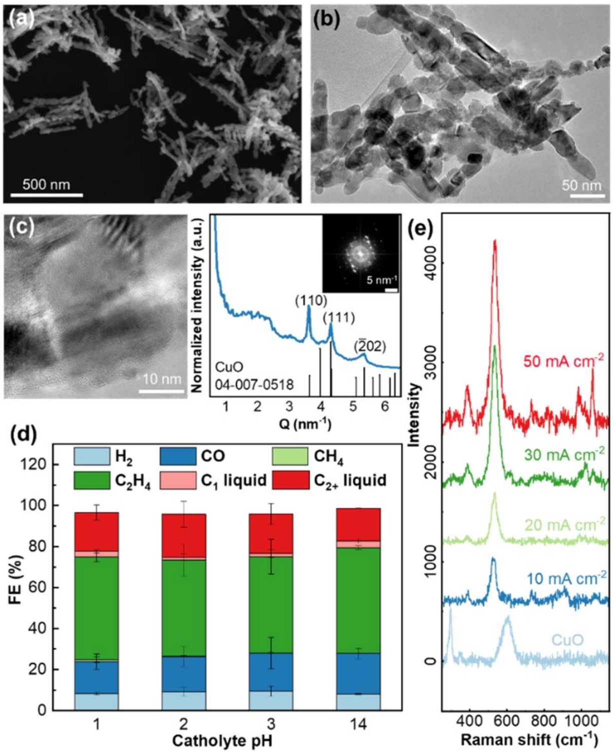

Fig. 1 Acidic CO_2 reduction reaction (CO_2RR) over CuO catalysts. (a) SEM image (scale bar: 500 nm), (b) bright-field TEM image, and (c) high-resolution TEM image with the corresponding FFT pattern and its rotationally averaged intensity profile of the synthesised CuO catalysts. (d) Product distribution of flow-cell CO_2RR at 600 mA cm^{-2} and pH values of 1, 2, 3, and 14. (e) *Operando* Raman spectra of CuO at 10, 20, 30, and 50 mA cm^{-2} in a catholyte of pH 2.

the FE for H_2 remains stable with an increasing current density; the product distribution, however, shifts from CO to C_2H_4, likely due to higher overpotentials at elevated current densities (Fig. S2). The FE for C_{2+} products ranges from 45 to 55% at 200 mA cm^{-2} and increases to 65–75% at 800 mA cm^{-2} (Fig. S2). When operating the cell at high current densities (*e.g.*, 600 and 800 mA cm^{-2} at pH 1 and 800 mA cm^{-2} at pH 2), the FE for C_{2+} products exceeds 70% and approaches 76%, the value achieved with a flow cell using 1 M KOH.[19]

The product distribution in acidic electrolytes is notably similar to that observed in 1 M KOH using the same catalyst and experimental setup, suggesting that the local pH at the reaction sites is alkaline even when an acidic catholyte is used. The alkaline surface pH is further confirmed by the presence of the $CuO_x/(OH)_y$ peak in the *operando* Raman spectra, acquired at current densities ranging from 10 to 50 mA cm^{-2} to minimise the accumulation of gas bubbles on the GDE surface (Fig. 1e). At an applied current density of 10 mA cm^{-2}, one can note the disappearance of the characteristic CuO phase peaks at 298 and 348 cm^{-1} and that of a broad peak at 540–660 cm^{-1}, along with the appearance of the $CuO_x/(OH)_y$ peak at 385–390 and 525–535 cm^{-1}.[32] When probing at the same location on the GDE, the area under the $CuO_x/(OH)_y$ peak increases correspondingly as the current density is raised to 20, 30, and 50 mA cm^{-2}, indicating a higher concentration of OH^-. Peaks corresponding to the bicarbonate and carbonate phases at 1020 and 1060 cm^{-1} begin to appear at current densities above 30 mA cm^{-2}, confirming the reaction between CO_2 and local OH^- to form adsorbed bicarbonate and carbonate species.[33,34] The alkaline surface pH, as demonstrated in previous studies, is favourable for C–C coupling and C_{2+} product formation, explaining the observed selectivity towards C_{2+} products despite the use of an acidic catholyte.[35] Varying the CO_2 flow rate between 14.5 and 62.9 mL min^{-1} has a minimal effect on the CO_2RR selectivity in the catholyte at pH 2: the H_2 FE remains below 10%, while the C_{2+} FE lies between 63% and 70% (Fig. S3). The single-pass carbon conversion efficiency for C_{2+} products is 3.3% at a current density of 600 mA cm^{-2}, obtained at a CO_2 flow rate of 14.5 mL min^{-1} (SI S1).

Prolonged lifetime of carbon-based GDEs on a GNP-CuO scaffold

Under acidic CO_2RR conditions (pH 2) at 600 mA cm^{-2}, the lifetime of the CuO-GDE ranges from 3 to 4 hours using a single-pass catholyte setup, as demonstrated recently.[29] The CuO catalysts were mixed with 2D structured graphene nanoplatelets (GNPs) to extend the lifetime of the GDE. The CuO-GNP combinations were prepared at four different GNP : CuO mass ratios: 0.05 : 1, 0.1 : 1, 0.25 : 1, and 1 : 1. In all GNP-CuO combinations, the CuO loading was maintained at approximately 0.2 mg cm^{-2} in the preparation of the GDEs, as confirmed by inductively coupled plasma-optical emission spectroscopy (Table S1). The product selectivity of these GNP-CuO mixtures at 600 mA cm^{-2} is shown in Fig. 2a. All samples exhibit similar

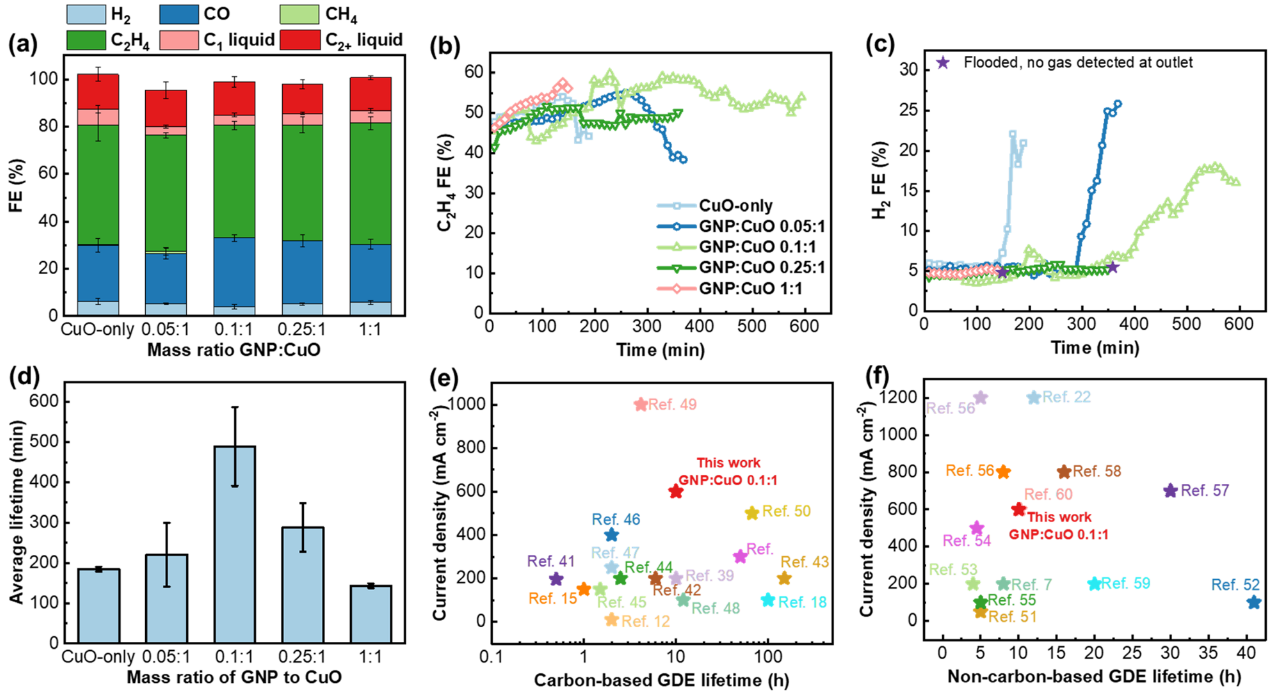

Fig. 2 Acidic CO_2RR selectivity and stability of CuO-only and GNP-CuO gas diffusion electrodes (GDEs). (a) Product distribution of flow-cell CO_2RR in the catholyte at pH 2 and 600 mA cm^{-2} for the CuO-only GDE and GNP-CuO GDEs with varying GNP-to-CuO mass ratios. Evolution of (b) C_2H_4 and (c) H_2 faradaic efficiency (FE) over time for the GNP-CuO GDEs; the curves correspond to the samples with the longest lifetimes. (d) Average lifetimes of CuO-only and GNP-CuO GDEs; the error bars represent standard deviations from at least three independent samples. Comparison of lifetime–current density merit of the GNP : CuO 0.1 : 1 GDE with values reported in the literature for (e) carbon-based and (f) non-carbon-based GDEs.

product distributions to the GDE loaded with 0.2 mg cm^{-2} of CuO. This indicates that the integration of GNP with CuO does not alter the CO$_2$RR selectivity and that CuO remains the primary active phase for the reaction. In a densely packed CL, for example one composed only of catalyst, it has previously been demonstrated that there are selectivity gradient zones within the CL.[36] The zone far from the MPL and close to the electrolyte mainly produces H$_2$ due to low CO$_2$ concentration and high proton activity, whereas the zone close to the MPL mainly produces C$_{2+}$ products due to the opposite trend. Similar significant changes in selectivity were observed with a dense CL composed solely of CuO catalysts; for example, the H$_2$ FE approximately doubled when the CuO loading increased from 0.2 to 1.25 mg cm^{-2} (Fig. S4). Here, the slight differences in selectivity observed when varying the GNP : CuO ratios further emphasize the advantage of the house-of-cards structure, highlighting that the role of the GNP is simply to disperse the same amount of catalyst within a thicker CL. The house-of-cards structure provided by the GNP further expands the interface between the catalyst, electrolyte, and CO$_2$ across the CL, enabling homogeneous selectivity throughout the catalyst layer thickness.

Fig. 2b and c show the C$_2$H$_4$ and H$_2$ selectivities over time for GDEs with different GNP-to-CuO ratios, and Fig. S5 presents the full product distributions. Two distinct deactivation modes were observed. The first is characterised by a gradual increase in the HER and a corresponding decrease in C$_2$H$_4$ production, as observed with the CuO-only composition and the GNP : CuO ratios of 0.05 : 1 and 0.1 : 1. This is attributed to catholyte penetration into the rear side of the GDE, which restricts CO$_2$ (reactant) access to the catalyst and promotes water splitting.[37,38] In the second deactivation mode, observed in the samples with GNP : CuO ratios of 0.25 : 1 and 1 : 1, the reaction was forced to stop after detecting no gas at the outlet. This is induced by salt crystal formation from the penetrated catholyte, which blocks the escape pathways for the gas products. As a result, these products are unable to diffuse through the GDE and reach the gas outlet. In this scenario, flooding occurs with no changes in the H$_2$ and C$_2$H$_4$ selectivities, as the blockage primarily affects the gas products rather than the CO$_2$ reactant. Both deactivation modes occur randomly across all samples, depending on the progression of catholyte seepage, and no specific mode can be consistently associated with a particular GNP-to-CuO ratio.

The addition of GNP improves the lifetime of the GDE without affecting the product selectivity (Fig. 2d). In this study, the average lifetime and standard deviation were calculated from at least three independent samples (Fig. S5–S10). The time at which the H$_2$ FE exceeds 20% was defined as the "dead time" of the GDE. The average GDE lifetime increases slightly from 185 minutes for the CuO-only system to 230 minutes for the sample with 5 wt% GNP, reaching a maximum of 490 minutes at 10 wt% GNP. However, further increases in the GNP content lead to a decline in the average lifetime, which drops to 290 and 140 minutes for the remaining (higher) GNP loadings. The lifetimes of carbon-based GDEs reported in the literature at different current densities for various catalysts are summarised in Fig. 2e,[12,15,18,39–50] with further details presented in Table S2. Stability tests on carbon-based GDEs are typically conducted at current densities between 100 and 200 mA cm^{-2}, with the lifetime reaching 150 hours at 200 mA cm^{-2}. In comparison, our GNP : CuO 0.1 : 1 sample demonstrates a carbon-based GDE lifetime of 10 hours at a significantly higher current density of 600 mA cm^{-2} (Fig. S5), outperforming many GDEs from previous studies that achieved similar lifetimes though at lower current densities (100–200 mA cm^{-2}). This lifetime–current density merit is comparable to that of other PTFE-based GDEs and self-supported porous Cu GDEs, which are generally more durable than carbon-based ones (Fig. 2f).[7,22,51–60] Further details are provided in Table S3. Notably, our CuO loading is only 0.2 mg cm^{-2}, and further optimisation of the GNP : CuO 0.1 : 1 surface loading may prolong the GDE lifetime.

To elucidate the degradation mechanism in the CuO and GNP-CuO GDEs, the reaction time was fixed at 150 minutes. This duration is shorter than the lifetimes of the two less durable samples (CuO and GNP : CuO 1 : 1) yet sufficiently long to observe differences in the GDEs after operation under CO$_2$RR conditions at 600 mA cm^{-2}. We first evaluated the degree of flooding based on the change in mass of the GDE, which reflects the amount of salt retained in the pores of the CL, MPL, and GDL. After a reaction time of 150 minutes, the used GDE was rinsed on the catalyst side to remove residual electrolyte and on the backside to eliminate large droplets that had fully crossed over and visible salt crystals. This procedure ensured that only the salt that had infiltrated into the pore structure was evaluated. Only a 0.26 mg increase in mass can be observed for GNP : CuO 0.1 : 1, indicating minimal flooding in this sample (Fig. 3a). Slightly higher mass changes were observed for GNP : CuO 0.05 : 10 (0.53 mg) and GNP : CuO 0.25 : 1 (0.79 mg). The most severe flooding, as indicated by the highest mass gains, is exhibited by the CuO-only (1.75 mg) and GNP : CuO 1 : 1 (1.98 mg) samples. All samples initially exhibit a similar degree of hydrophobicity, as reflected by the water contact angles (WCAs), ranging from 153° to 158° (Fig. S11 and S12). However, after a reaction time of 150 minutes at a current density of 600 mA cm^{-2}, the loss in hydrophobicity varies among the samples (Fig. 3b and S13–S17). Fig. 3c presents the average WCA, measured at three (at the minimum) different locations (Fig. S13–S17) on the used GDE. In the GNP : CuO 0.1 : 1 sample, the WCA remains relatively high (136°). In contrast, the WCA decreases to 81.5°, 86.6°, and 80.8° for the GNP : CuO ratios of 0.05 : 1, 0.25 : 1, and 1 : 1, respectively. The most significant loss in hydrophobicity was observed for the CuO-only sample, with a WCA of only 52°. This reduction in hydrophobicity is closely correlated with the mass gain due to flooding, suggesting that a greater loss in hydrophobicity is a key factor contributing to more severe flooding in the GDE.

The quantitative mapping of Cu and K across the cross-section of the used GDEs after 150 minutes at 600 mA cm^{-2} reveals the degree of flooding (Fig. 3d; the back-scattered electron images and EDX acquisition areas are presented in Fig. S18), consistent with the mass gain data, and reflects the concentration distribution of each element. In the concentration maps for the CuO-only and GNP : CuO 1 : 1 samples, K

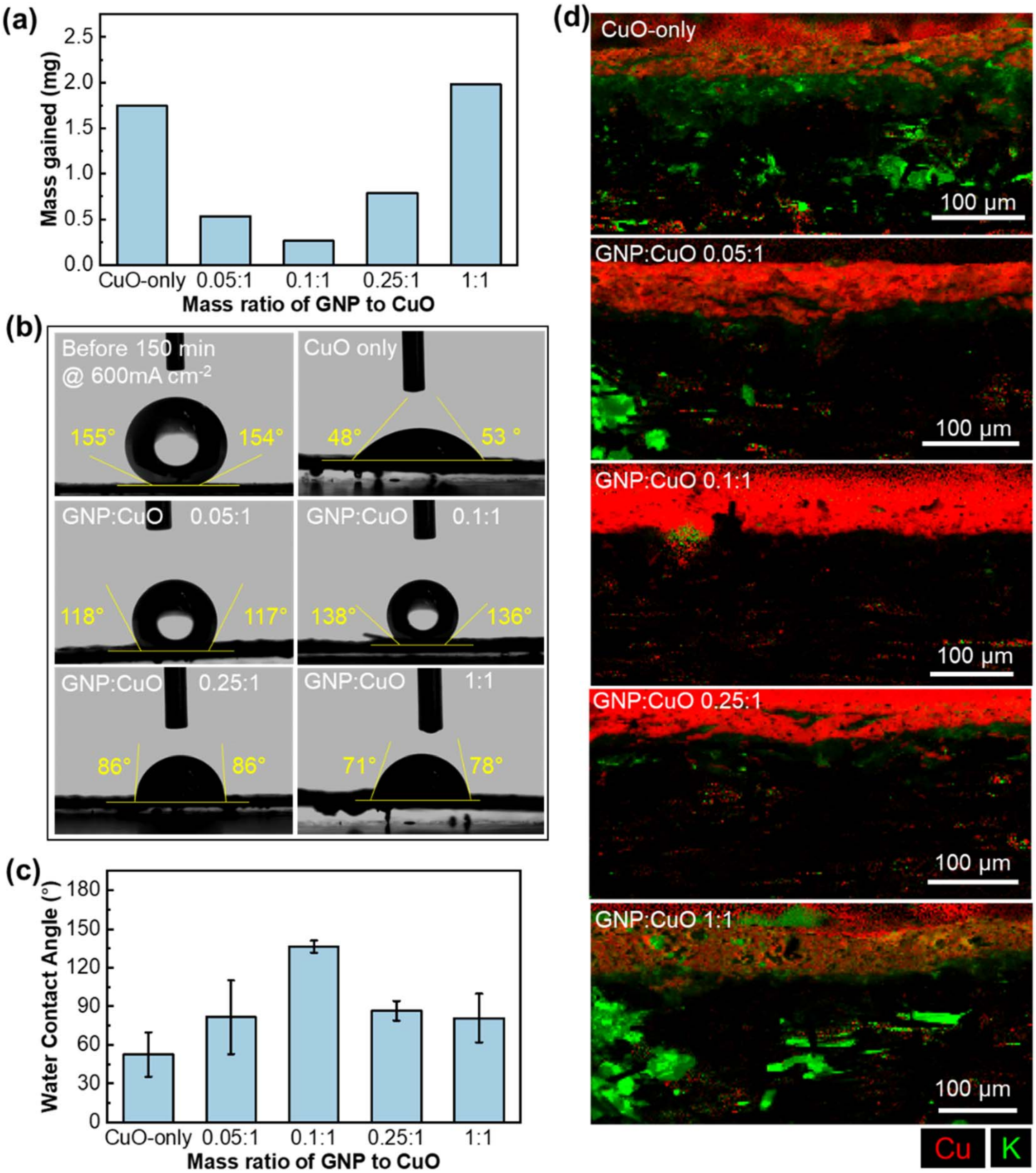

Fig. 3 GDE characterisation after a reaction time of 150 minutes at 600 mA cm^{-2} (pH 2) to assess flooding. (a) Mass gain of the used GDEs after a 150 minute reaction compared to that of the as-prepared GDEs. (b) Water contact angles (WCAs) of as-prepared CuO-only GDEs and CuO-only and GNP-CuO GDEs after a reaction time of 150 minutes. (c) Average WCAs of CuO-only and GNP-CuO GDEs after a reaction time of 150 minutes; the error bars represent standard deviations from at least three independent regions. (d) Quantitative mapping of Cu and K across the cross-section of the used GDEs after a reaction time of 150 minutes.

penetrates completely through the entire mass of the GDE. In some regions, large salt deposits are visible within the GDL. In the GNP : CuO 0.05 : 1 sample, similar salt blocks are present, but they are more localised compared to the widespread K distribution observed in the CuO-only and GNP : CuO 1 : 1 samples (where K extends from the CL through the MPL to the GDL). In the GNP : CuO 0.25 : 1 sample, no significant K presence was detected in the GDL; however, the electrolyte has noticeably penetrated through the CL and reached the MPL. The least-flooded GDE is GNP : CuO 0.1 : 1, where K is confined to the CL, with a negligible presence in both the MPL and GDL. Count intensity maps acquired from two additional regions of the used GDEs show a similar trend (Fig. S19–S23). Notably, Cu was also detected in the cross-sections, possibly due to dynamic catalyst relocation *via* a dissolution–redeposition process.[37]

Considering the results thus far, the flooding resistance of the GDE is improved by the addition of GNP, with the optimal resistance observed at a GNP : CuO mass ratio of 0.1 : 1. However, increasing the GNP content beyond this ratio results in reduced flooding resistance. To elucidate this trend, it is necessary to examine both the structure of the CL and the CO_2 diffusion process for various amounts of GNP added to a fixed CuO loading of 0.2 mg cm^{-2} on the GDE. A custom-made cell for evaluating CO_2 permeation through the GDE is illustrated in

Fig. 4a, consisting of an H-cell with two compartments, where the GDE sample is placed between them using two rubber gaskets to create gas- and liquid-tight seals. In the compartment exposing the rear side of the GDE, CO_2 gas is introduced in a flow-by configuration. In the opposite compartment exposing the CL, a fixed volume of water is added, followed by the insertion of a dissolved CO_2 probe. This design closely mimics the flow-by mode of a typical flow cell and enables the measurement of CO_2 diffusing through the GDE and dissolving in the liquid phase. The CL thickness was determined from the chemical contrast observed in the BSE-SEM images of the GDE cross-section, with the bright layer corresponding to the CuO-containing CL (Fig. S24).

The concentration of dissolved CO_2 in the liquid compartment of the cell increases over time, rising from the ambient level of approximately 400 ppm to a saturation plateau of around 1600 ppm, close to the solubility limit of 33 mmol L^{-1} (Fig. 4b). With the addition of approximately 5 wt% GNP to the CuO catalyst (with the CuO loading fixed at 0.2 mg cm^{-2} for all samples), the time required to reach 1500 ppm of dissolved CO_2 is reduced from 39 minutes to a mere 16 minutes (Fig. 4c). An increase in the CL thickness from 18 to 33 μm can be noted (Fig. 4d and e), suggesting that the inclusion of GNP leads to a more porous, less dense structure. Upon increasing the GNP : CuO mass ratio to 0.1 : 1 (approximately 9%), the time required to reach 1500 ppm of dissolved CO_2 rises to 22 minutes. This increase can be attributed to a thicker CL (rising from 33 to 48 μm), thereby creating a longer diffusion path for CO_2. Within this low-GNP mass range (up to 9 wt%), it is likely that the 2D structure of GNP forms a scaffolded, house-of-cards-like architecture. This structure introduces additional voids within the CL, promoting more effective CO_2 diffusion than a densely packed CuO-only layer, as evidenced by the top-view BSE-SEM images of the GDE (Fig. S25).

Increasing the GNP content to 20 wt% (GNP : CuO 0.25 : 1) results in reduced CO_2 permeation, with the time to reach 1500 ppm increasing to 26 minutes. Interestingly, the CL thickness decreases slightly to 39 μm, suggesting a densification of the CL. At the highest GNP loading of 50 wt% (GNP : CuO 1 : 1), the CL thickness remains almost unchanged (42 μm, but within the error bar). However, the time required to reach 1500 ppm increases further to 32 minutes, indicating a continued loss of CO_2 permeability. This progressive densification at higher GNP loadings is likely due to the excessive amount of 2D GNP sheets. While a low GNP : CuO ratio can create a loosely packed, scaffold-like architecture with additional voids and enhance CO_2 diffusion, a higher ratio leads to the stacking and aggregation of the GNP sheets. The porous, percolated network obtained with a GNP ratio lower than 9 wt%

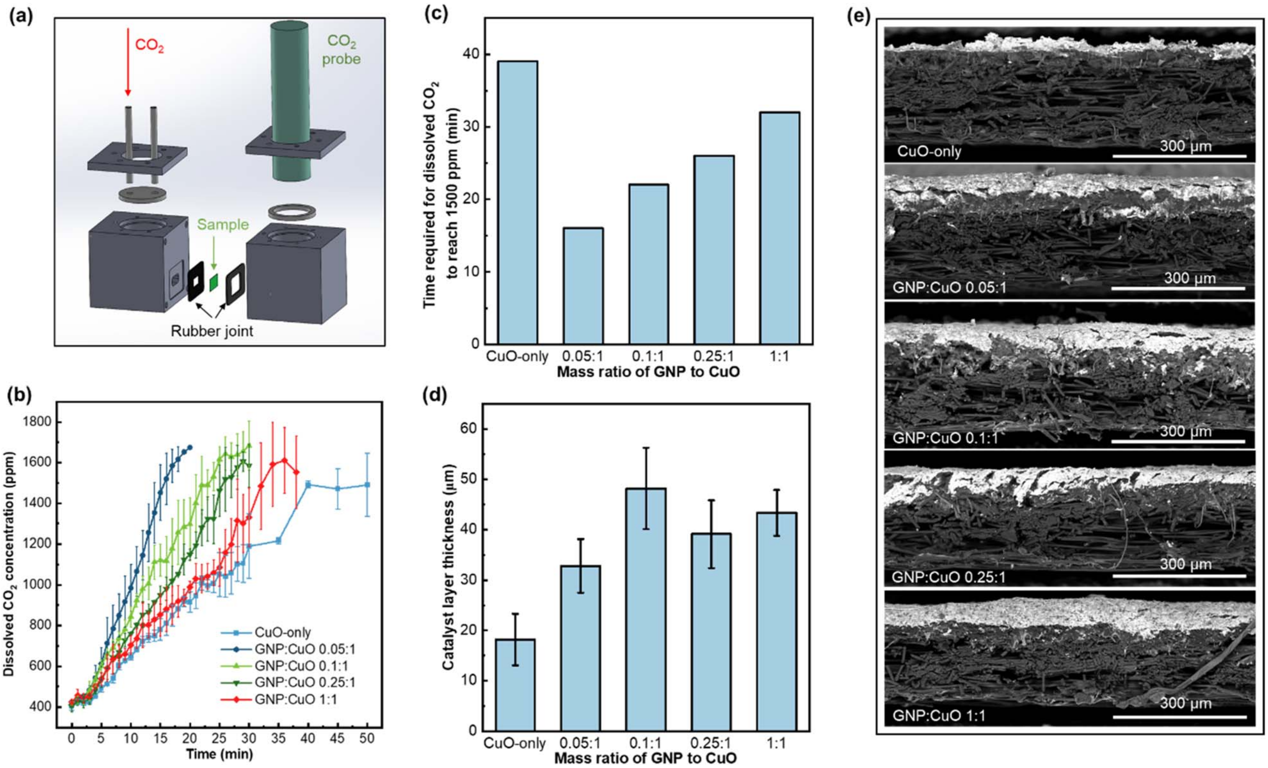

Fig. 4 Balancing CO_2 transport and flooding accommodation in CuO-only and GNP-CuO GDEs. (a) Design of the custom-made cell for measuring the CO_2 diffusion time. (b) Measurement of dissolved CO_2 transport across the GDEs in a flow-by configuration. (c) Time required for dissolved CO_2 to reach 1500 ppm. (d) Average catalyst layer (CL) thickness determined from backscattered electron (BSE)-SEM images; the error bars represent standard deviations from at least six independent regions. (e) Representative BSE-SEM images highlighting the chemical contrast for determining the CL thickness.

is replaced by a more compact, less permeable structure that hinders effective CO_2 mass transport through the GDE.

Considering these observations, the longest lifetime, achieved with a GNP : CuO ratio of 0.1 : 1, was attributed to a thick CL exhibiting a house-of-cards structure. A thick CL with a high void fraction provides more space to accommodate catholyte seepage while still ensuring the sufficient diffusion of CO_2 throughout the layer. Simply increasing the thickness of the CL (from 18 to 27 μm) by raising the catalyst loading (from 0.2 to 0.34 mg cm^{-2}) can increase the GDE lifetime (Fig. S26); however, an excessive loading (1.3 mg cm^{-2} and a corresponding CL thickness of 56 μm) leads to higher selectivity towards the HER and a reduced resistance to flooding (Fig. S27). By incorporating a scaffold phase (2D structure), a comparable thickness of 48 μm (compared to 56 μm obtained with a CuO loading of 1.3 mg cm^{-2}) can be achieved with a minimal catalyst loading of only 0.2 mg cm^{-2} and a scaffold phase loading of 0.02 mg cm^{-2}.

Regulation of reaction interfaces by GDE microstructure

In a GDE, the equilibrium at the gas–liquid interface (where the CO_2 reduction reaction occurs) is governed by the gas-phase pressure, liquid-phase pressure, and capillary pressure, which is determined by the pore size and surface wettability.[11,24,38,61] In the hydrophobic components of the GDE, such as the MPL and the GDL, flooding is resisted by the capillary pressure: only when the differential between the liquid- and gas-phase pressure across the electrode exceeds the capillary pressure threshold can the electrolyte invade the pores. Small pores in hydrophobic materials create a higher capillary pressure, thus providing greater resistance to flooding. For the CL, it should have sufficient wettability to enable proton supply to the reaction sites and provide sinks for liquid products. The CL also needs to maintain adequate CO_2 diffusion within its structure to ensure sufficient reactant availability. The CL must not become completely flooded to avoid shifting the gas–liquid interface towards the MPL side and limiting CO_2 access to the catalyst. Ideal wetting is achieved by coating the catalyst particles with a thin layer of a hydrophobic binder; this covers the catalyst surface with an electrolyte film for supplying protons, providing sinks for liquid products, and enabling ionic buffering, while the remaining voids ensure CO_2 diffusion. Similar to the MPL, small pores can be beneficial for the CL by increasing the capillary threshold when the CL is partially hydrophobic. However, pore volume is also important for accommodating liquid seepage, and increasing pore volume solely by increasing catalyst loading may lead to large gradients between different selectivity zones.[36] Therefore, creating a house-of-cards structure through GNP incorporation enables higher pore volume while extending the mixed interface between the catalyst, electrolyte, and CO_2 throughout the CL.

Resistance to flooding can be further enhanced *via* the microstructuring of the CL architecture, by tuning the pore properties to facilitate CO_2 transport and accommodate liquid seepage. For a dense and thin CL composed of only CuO (0.2 mg cm^{-2}), the CL is likely to become fully flooded when electrowetting occurs, as the capillary force draws liquid into the small pores. Provided that CO_2 access to catalytic sites remains sufficient, increasing the catalyst loading (CuO-only, 0.34 mg cm^{-2}) can act as a physical barrier to flooding since the additional material may reduce the pore connectivity and increase the total pore volume, slowing down electrolyte intrusion. However, for excessively high catalyst loadings (CuO-only, 1.3 mg cm^{-2}), an extensively thick barrier results in a reduced buffering capacity,[36] which leads to the accumulation of OH^- ions at the gas–liquid interface (now located closer to the MPL) and severe flooding. Furthermore, while reduced pore connectivity hinders liquid intrusion, it also limits CO_2 access, as reflected by the increased FE for H_2. The incorporation of an inert, 2D phase at an appropriate mass ratio can modify the pore connectivity and pore volume of the CL, thereby altering the tortuosity and liquid distribution within the CL, as illustrated in Fig. 5. Upon the addition of 5 wt% GNP (GNP : CuO mass ratio = 0.05 : 1), the CL thickness doubles, while the time required to reach a saturated CO_2 concentration is reduced by half. This suggests that the addition of GNP modifies the pore structure of the CL, likely reducing tortuosity and allowing CO_2 to diffuse more rapidly through a thicker CL. These results support the formation of a house-of-cards architecture introduced by the GNP, which improves the pore connectivity and increases the pore volume. Upon increasing the GNP content to 9 wt% (GNP : CuO ratio = 0.1 : 1), the time required for CO_2 to diffuse through the entire GDE increases, most likely due to the longer diffusion path associated with the thicker CL. We concluded that the house-of-cards structure is preserved at these two GNP percentages, as the CL thickness increases with the GNP : CuO ratio. With a thicker CL maintaining this architecture, the CO_2 diffusion time becomes longer because of the increased travel distance, though an increased void volume is available to accommodate electrolyte seepage. The GNP : CuO mass ratio of 0.1 : 1 represents an optimal balance between CO_2 diffusion and liquid intrusion, enabling a maximal GDE lifetime. Further increases in the GNP content (GNP : CuO ratios of 0.25 : 1 and 1 : 1) lead to longer diffusion times, even though the CL thickness remains unchanged. This suggests an increase in tortuosity, forcing CO_2 to travel across a more convoluted path within the CL. The addition of material with no accompanying increase in the CL thickness indicates the densification of the CL. Specifically, excessive GNP partially disrupts the anisotropic arrangement as in the house-of-cards structure, resulting in a more isotropic, in-plane ordering. This arrangement increases the CL tortuosity and may block pores, hindering CO_2 access. Moreover, densification reduces the volume of void space available to accommodate electrolyte seepage, which explains the observation of a reduced GDE lifetime at GNP contents above 9 wt%.

Methods

Synthesis of CuO catalysts & preparation of GDEs

The Cu-based catalysts were synthesised using a similar protocol as previously reported.[19] Briefly, 1.3 g of $Cu(NO_3)_2 \cdot 3H_2O$ (Sigma-Aldrich) was dissolved in 100 mL of Milli-Q water, after which 30 mL of 0.15 M NH_4OH prepared from ammonium

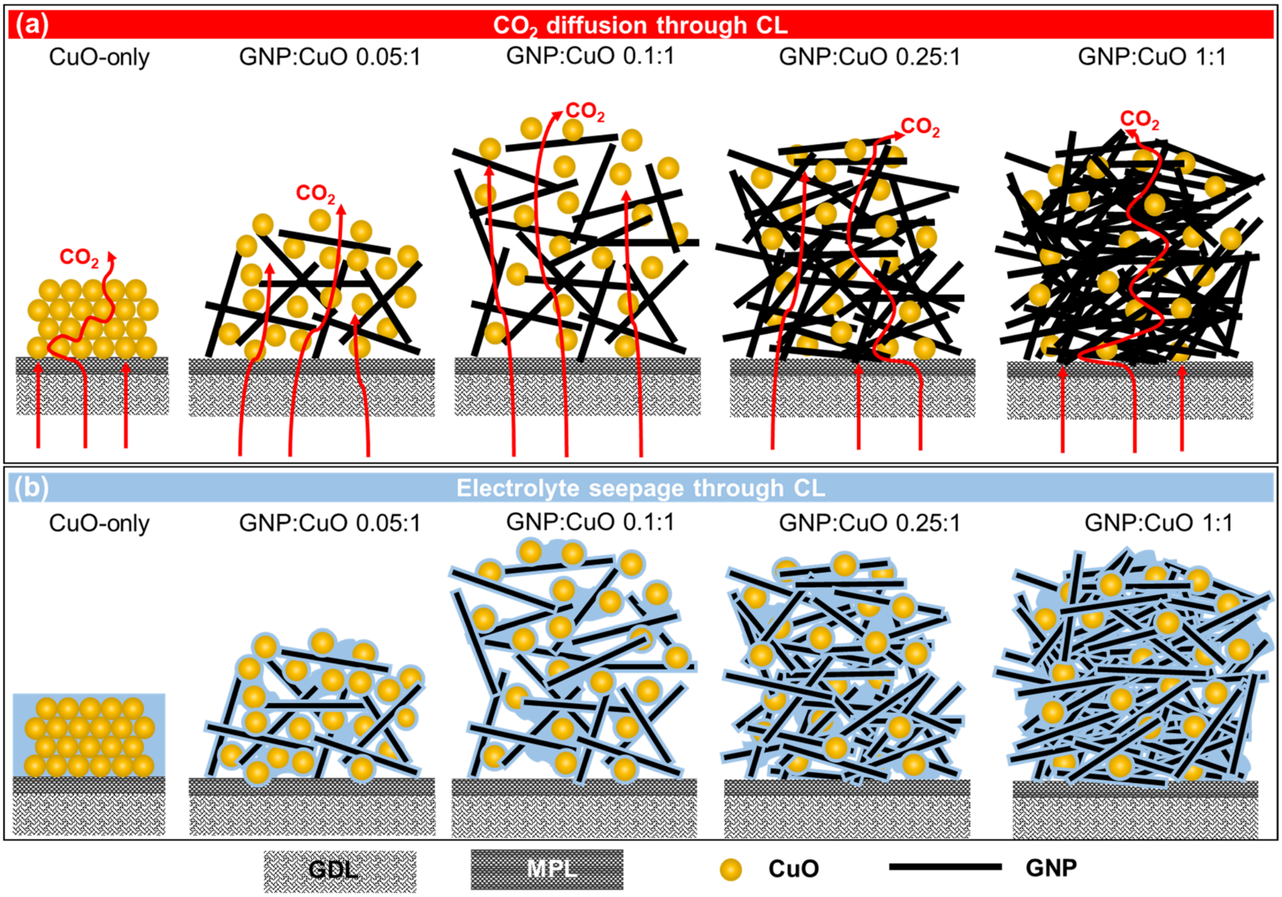

Fig. 5 Schematic (not drawn to scale) of the CL cross-section for the CuO-only GDE and GNP-CuO GDEs at various GNP-to-CuO mass ratios, based on a constant CuO catalyst loading across all samples; the differences in the CL thickness reflect observations from SEM cross-sectional imaging. (a) Illustration of the CL structure and tortuosity relevant to CO_2 diffusion. (b) Depiction of wetting behaviour within the CLs, highlighting the free volume available to accommodate electrolyte seepage.

hydroxide (28% NH_3, Alfa Aesar), was added. Subsequently, 10 mL of 1.0 M NaOH (Reactolab SA) was introduced dropwise at 2 mL min^{-1} under continuous magnetic stirring to induce $Cu(OH)_2$ precipitation. The mixture was stirred for 30 min, and the resulting precipitate was collected by centrifugation, filtered, and washed sequentially with deionised water and ethanol. The washed solid was freeze-dried for 72 h and calcined in air at 300 °C for 1 h to obtain CuO catalysts.

Catalyst inks were prepared by dispersing 4 mg of the as-synthesised CuO (for CuO-only inks) or 4 mg of the CuO/GNP composite powder in 1 mL isopropanol. To this dispersion, 16 µL of a 5 wt% PTFE suspension (diluted from a 65 wt% stock (Fuel Cell Store)) was introduced. The ink was spray-coated onto as-received gas diffusion electrodes (YLS-30T, Suzhou Sinero Technology Co.) to reach theoretical CuO loading of 4 mg per 10 cm^2. After solvent evaporation, the coated GDEs were calcined in air at 300 °C for 30 min to melt the PTFE and achieve a uniform, conformal coating over the catalyst layer.

Electrochemical characterizations & products quantification

Electrochemical tests were conducted using a potentiostat (Metrohm Autolab PGSTAT302N). Gaseous products were quantified in real time *via* an online gas chromatograph (SRI Instruments 8610C) equipped with both a thermal conductivity detector and a flame ionisation detector. Upon completion of chronopotentiostatic runs, the electrolyte was collected for analysis of liquid products by 1H nuclear magnetic resonance (1H NMR; Bruker 400 MHz AVIII HD) spectroscopy.

Electrolysis was performed in a single-pass flow cell setup identical to that described in previous work,[29] featuring a cation-exchange membrane (Nafion 115, Ion Power) separating cathode and anode compartments. The electrode area exposed to electrolyte was 0.5 cm^2. A leakless Ag/AgCl reference electrode (Metrohm) and a platinum plate counter electrode were used. The catholyte consisted of 3 M KCl (Sigma-Aldrich), with pH adjusted to 2 *via* addition of 3 M H_3PO_4 (diluted from 85%, Sigma-Aldrich). The anolyte was a 3 M $KHCO_3$ solution (Thermo Scientific).

Material characterizations

Scanning electron microscopy (SEM) and energy-dispersive X-ray (EDX) elemental mapping were performed on a FE-SEM (ThermoFisher Teneo). Bright-field and high-resolution transmission electron microscopy (HR-TEM) images were acquired on a ThermoFisher Tecnai Osiris operated at 200 kV. Elemental compositions were quantified by inductively coupled plasma-optical emission spectrometry (ICP-OES; Agilent 5110). *Operando* Raman spectroscopy was conducted in a custom semi-flow cell under continuous CO_2 gas flow. The catholyte comprised 3 M KCl, acidified to pH 2 with 3 M H_3PO_4, while the anolyte consisted of 3 M $KHCO_3$. Both electrolytes remained static during measurement. A Leica 63× immersion objective was used for signal collection, with excitation from a 632 nm laser. Water contact angles were measured using a Krüss EasyDrop Drop Shape Analyser. CO_2 permeation measurements were performed using a dissolved-CO_2 probe (BGT Technology, Beijing).

Conclusion

In summary, this study confirmed the formation of C_{2+} products in the CO_2RR under acidic conditions, driven by a high local alkalinity at the catalyst surface. However, this also induced the flooding of the GDE, despite the acidic bulk electrolyte. Introducing a loosely packed CL with a high void fraction and partial wettability, termed the "house-of-cards" structure, showed promise in mitigating flooding. This structure was obtained by incorporating GNPs – a 2D, nonreactive material – into the catalyst ink, followed by spray-coating onto the GDE. For a GNP content below 9 wt%, a house-of-cards structure was successfully formed, as evidenced by an increased CL thickness and a reduced CO_2 diffusion time through the layer. At a GNP mass fraction of 9% (GNP : CuO mass ratio = 0.1 : 1), the GDE lifetime reached 10 hours at a current density of 600 mA cm^{-2}, attributed to an optimal CL structure that balanced CO_2 transport with the void volume to accommodate electrolyte seepage. Higher GNP fractions induced CL densification, reducing the void volume and CO_2 diffusion and shortening the GDE lifetime. This microstructural design of the CL complements ongoing research efforts on the microporous and gas diffusion layers, offering a viable approach to enhancing the flooding resistance of GDEs.

Author contributions

T. H. M. Pham: conceptualization, formal analysis, investigation, methodology, validation, writing – original draft. J. Zhang: investigation, methodology, writing – review & editing. L. Lombardo: investigation, methodology, writing – review & editing. A. Züttel: project administration, resources, supervision.

Conflicts of interest

There are no conflicts to declare.

Data availability

The data supporting this article have been included as part of the supplementary information (SI). Supplementary information: equations for calculations, ICP/OES analysis, SEM images and the corresponding EDX maps, GDE cross-section analysis, electrochemical and selectivity data, contact angle images, references for lifetime comparison. See DOI: https://doi.org/10.1039/d6ta00347h.

Acknowledgements

The authors acknowledge the financial support of EPFL, EMPA. We thank Robin Délèze for fabricating the CO_2-diffusion cell and for providing Fig. 4a. We also thank Dr Aurélien Bornet for assistance with NMR for liquid product quantification, Stéphane Voeffray for assistance with the *operando* Raman cell, and Dr Emad Oveisi for discussions on cross-sectional SEM imaging.

Notes and references

1 M. Potter, D. E. Smith, C. G. Armstrong and K. E. Toghill, *EES Catal.*, 2024, **2**, 379–388.
2 A. Anzai, M. Higashi and M. Yamauchi, *Chem. Commun.*, 2023, **59**, 11188–11191.
3 T. Ito, J. Raj, T. Zhang, S. Roy and J. Wu, *EES Catal.*, 2024, **2**, 997–1005.
4 S. Nitopi, E. Bertheussen, S. B. Scott, X. Liu, A. K. Engstfeld, S. Horch, B. Seger, I. E. L. Stephens, K. Chan, C. Hahn, J. K. Nørskov, T. F. Jaramillo and I. Chorkendorff, *Chem. Rev.*, 2019, **119**, 7610–7672.
5 Y. Hori, *Mod. Aspect. Electrochem.*, 2008, **42**, 89–189.
6 J. Zhang, T. H. M. Pham, S. Xi, L. Zhong, D. Liem, F. You, B. Rowley, R. Ganganahalli, F. Calle-Vallejo and B. S. Yeo, *J. Mater. Chem. A*, 2024, 31547–31556.
7 A. Perazio, C. E. Creissen, J. G. Rivera de la Cruz, M. W. Schreiber and M. Fontecave, *ACS Energy Lett.*, 2023, **8**, 2979–2985.
8 F. P. García de Arquer, C. T. Dinh, A. Ozden, J. Wicks, C. McCallum, A. R. Kirmani, D. H. Nam, C. Gabardo, A. Seifitokaldani, X. Wang, Y. C. Li, F. Li, J. Edwards, L. J. Richter, S. J. Thorpe, D. Sinton and E. H. Sargent, *Science*, 2020, **367**, 661–666.
9 T. Burdyny, *Nat. Chem. Eng.*, 2025, **2**, 350–357.
10 Y. Wu, H. Rabiee, X. S. Zhao, G. Wang and Y. Jiang, *J. Mater. Chem. A*, 2024, **12**, 14206–14228.
11 M. Li, M. N. Idros, Y. Wu, T. Burdyny, S. Garg, X. S. Zhao, G. Wang and T. E. Rufford, *J. Mater. Chem. A*, 2021, **9**, 19369–19409.
12 K. Yang, R. Kas, W. A. Smith and T. Burdyny, *ACS Energy Lett.*, 2021, **6**, 33–40.
13 L. M. Baumgartner, C. I. Koopman, A. Forner-Cuenca and D. A. Vermaas, *ACS Appl. Energy Mater.*, 2022, **5**, 15125–15135.
14 A. A. Samu, I. Szenti, Á. Kukovecz, B. Endrődi and C. Janáky, *Commun. Chem.*, 2023, **6**, 1–9.
15 Y. Wu, S. Garg, M. Li, M. N. Idros, Z. Li, R. Lin, J. Chen, G. Wang and T. E. Rufford, *J. Power Sources*, 2022, **522**, 230998.

16 S. Hao, A. Elgazzar, N. Ravi, T. U. Wi, P. Zhu, Y. Feng, Y. Xia, F. Y. Chen, X. Shan and H. Wang, *Nat. Energy*, 2025, **10**, 266–277.

17 B. Kim, F. Hillman, M. Ariyoshi, S. Fujikawa and P. J. A. Kenis, *J. Power Sources*, 2016, **312**, 192–198.

18 Y. Wu, L. Charlesworth, I. Maglaya, M. N. Idros, M. Li, T. Burdyny, G. Wang and T. E. Rufford, *ACS Energy Lett.*, 2022, **7**, 2884–2892.

19 T. H. M. Pham, J. Zhang, M. Li, T. H. Shen, Y. Ko, V. Tileli, W. Luo and A. Züttel, *Adv. Energy Mater.*, 2022, **12**, 2103663.

20 Z. Xing, L. Hu, D. S. Ripatti, X. Hu and X. Feng, *Nat. Commun.*, 2021, **12**, 1–11.

21 T. Zhang, Z. Li, X. Lyu, J. Raj, G. Zhang, H. Kim, X. Wang, S. Chae, L. Lemen, V. N. Shanov and J. Wu, *J. Electrochem. Soc.*, 2022, **169**, 104506.

22 J. E. Huang, F. Li, A. Ozden, A. S. Rasouli, F. P. G. de Arquer, S. Liu, S. Zhang, M. Luo, X. Wang, Y. Lum, Y. Xu, K. Bertens, R. K. Miao, C. T. Dinh, D. Sinton and E. H. Sargent, *Science*, 2021, **372**, 1074–1078.

23 J. A. Abarca, L. Warmuth, A. Rieder, A. Dutta, S. Vesztergom, P. Broekmann, A. Irabien and D. Guillermo, *ACS Catal.*, 2025, **15**, 8753–8767.

24 N. T. Nesbitt, T. Burdyny, H. Simonson, D. Salvatore, D. Bohra, R. Kas and W. A. Smith, *ACS Catal.*, 2020, **10**, 14093–14106.

25 Q. Wan, L. Yuan, W. Jiang, Y. Liu, L. Zhang, X. Zhuang, J. Zhang and C. Ke, *ACS Sustain. Chem. Eng.*, 2023, **11**, 17046–17052.

26 L. Li, J. Chen, V. S. S. Mosali, Y. Liang, A. M. Bond, Q. Gu and J. Zhang, *Angew. Chem., Int. Ed.*, 2022, **61**, e202208534.

27 S. Kwon, J. Zhang, R. Ganganahalli, S. Verma and B. S. Yeo, *Angew. Chem.*, 2023, **135**, 1–7.

28 J. J. Lv, M. Jouny, W. Luc, W. Zhu, J. J. Zhu and F. Jiao, *Adv. Mater.*, 2018, **30**, 1803111.

29 T. H. M. Pham, J. Zhang, W. Luo, B. S. Yeo and A. Züttel, *Carbon Energy*, 2025, **7**, e70075.

30 M. C. O. Monteiro, F. Dattila, B. Hagedoorn, R. García-Muelas, N. López and M. T. M. Koper, *Nat. Catal.*, 2021, **4**, 654–662.

31 J. Gu, S. Liu, W. Ni, W. Ren, S. Haussener and X. Hu, *Nat. Catal.*, 2022, **5**, 268–276.

32 Y. Zhao, X. Chang, A. S. Malkani, X. Yang, L. Thompson, F. Jiao and B. Xu, *J. Am. Chem. Soc.*, 2020, **142**, 9735–9743.

33 S. Jiang, K. Klingan, C. Pasquini and H. Dau, *J. Chem. Phys.*, 2019, **150**, 41718.

34 D. A. Henckel, M. J. Counihan, H. E. Holmes, X. Chen, U. O. Nwabara, S. Verma, J. Rodríguez-López, P. J. A. Kenis and A. A. Gewirth, *ACS Catal.*, 2021, **11**, 255–263.

35 C. Dinh, T. Burdyny, G. Kibria, A. Seifitokaldani, C. M. Gabardo, F. P. G. De Arquer, A. Kiani, J. P. Edwards, P. De Luna, O. S. Bushuyev, C. Zou, R. Quintero-bermudez, Y. Pang, D. Sinton and E. H. Sargent, *Science*, 2018, **787**, 783–787.

36 T. Mo, T. N. Thanh, X. Wang and P. Strasser, *Energy Environ. Sci.*, 2021, 5995–6006.

37 D. Takamatsu, N. Fukatani, A. Yoneyama, T. Hirano, K. Hirai, S. Yabuuchi, K. Watanabe, K. Kamiya and S. Nakanishi, *J. Am. Chem. Soc.*, 2025, **147**, 24103–24112.

38 L. M. Baumgartner, C. I. Koopman, A. Forner-Cuenca and D. A. Vermaas, *ACS Appl. Energy Mater.*, 2022, **5**, 15125–15135.

39 Y. C. Tan, K. B. Lee, H. Song and J. Oh, *Joule*, 2020, **4**, 1104–1120.

40 Z. Yao and R. Lin, *Small*, 2023, 1–8.

41 M. E. Leonard, L. E. Clarke, A. Forner-Cuenca, S. M. Brown and F. R. Brushett, *ChemSusChem*, 2020, **13**, 400–411.

42 E. R. Cofell, U. O. Nwabara, S. S. Bhargava, D. E. Henckel and P. J. A. Kenis, *ACS Appl. Mater. Interfaces*, 2021, **13**, 15132–15142.

43 J. Chen, H. Qiu, Y. Zhao, H. Yang, L. Fan, Z. Liu, S. B. Xi, G. Zheng, J. Chen, L. Chen, Y. Liu, L. Guo and L. Wang, *Nat. Commun.*, 2024, **15**, 5893.

44 N. B. D. Monti, G. A. El-Nagar, M. Fontana, F. Di Costola, S. Gupta, M. T. Mayer, C. F. Pirri and J. Zeng, *Mater. Today Sustain.*, 2025, **30**, 1–10.

45 M. van der Veer, N. Daems, P. Cool and T. Breugelmans, *Green Chem.*, 2025, **27**, 6039–6055.

46 D. Takamatsu, N. Fukatani, A. Yoneyama, T. Hirano, K. Hirai, S. Yabuuchi, K. Watanabe, K. Kamiya and S. Nakanishi, *J. Am. Chem. Soc.*, 2025, **147**, 24103–24112.

47 A. Alarcón, T. Andreu and C. Ponce de León, *Mater. Adv.*, 2024, **5**, 2377–2387.

48 P. Yue, Q. Fu, J. Li, L. Zhang, D. Ye, X. Zhu and Q. Liao, *ACS Appl. Mater. Interfaces*, 2023, **15**, 53429–53435.

49 A. Inoue, S. Nakasone, R. Yoshida, S. Nakahata, T. Harada, S. Nakanishi and K. Kamiya, *Small*, 2025, **21**, 1–10.

50 Q. Chen, Y. Tan, X. Wang, Q. Wang, H. Li, K. Liu, J. Fu, L. Chai, M. Liu and Z. Lin, *Nat. Commun.*, 2025, **16**, 1–10.

51 W. Nie, G. P. Heim, N. B. Watkins, T. Agapie and J. C. Peters, *Angew. Chem., Int. Ed.*, 2023, **91125**, 1–7.

52 A. Senocrate, F. Bernasconi, D. Rentsch, K. Kraft, M. Trottmann, A. Wichser, D. Bleiner and C. Battaglia, DOI:DOI: 10.1021/acsaem.2c03054.

53 F. Bernasconi, A. Senocrate and P. Kraus, *EES Catal.*, 2023, 1009–1016.

54 Y. Xie, P. Ou, X. Wang, Z. Xu, Y. C. Li, Z. Wang, J. E. Huang, J. Wicks, C. McCallum, N. Wang, Y. Wang, T. Chen, B. T. W. Lo, D. Sinton, J. C. Yu, Y. Wang and E. H. Sargent, *Nat. Catal.*, 2022, **5**, 564–570.

55 Q. Sun, Y. Zheng, J. Wang, Y. Ye, L. Fu, H. Xiong, H. Song, X. Chang and B. Xu, *J. Am. Chem. Soc.*, 2025, **147**, 21621–21628.

56 X. Zi, Y. Zhou, L. Zhu, Q. Chen, Y. Tan, X. Wang, M. Sayed, E. Pensa, R. A. Geioushy, K. Liu, J. Fu, E. Cortés and M. Liu, *Angew. Chem., Int. Ed.*, 2023, **62**, 1–7.

57 Z. Ma, Z. Yang, W. Lai, Q. Wang, Y. Qiao, H. Tao, C. Lian, M. Liu, C. Ma, A. Pan and H. Huang, *Nat. Commun.*, 2022, **13**, 1–11.

58 Y. Chen, X. Y. Li, Z. Chen, A. Ozden, J. E. Huang, P. Ou, J. Dong, J. Zhang, C. Tian, B. H. Lee, X. Wang, S. Liu, Q. Qu, S. Wang, Y. Xu, R. K. Miao, Y. Zhao, Y. Liu, C. Qiu,

J. Abed, H. Liu, H. Shin, D. Wang, Y. Li, D. Sinton and E. H. Sargent, *Nat. Nanotechnol.*, 2023, **19**, 311–318.

59 Y. Zhao, L. Hao, A. Ozden, S. Liu, R. K. Miao, P. Ou, T. Alkayyali, S. Zhang, J. Ning, Y. Liang, Y. Xu, M. Fan, Y. Chen, J. E. Huang, K. Xie, J. Zhang, C. P. O'Brien, F. Li, E. H. Sargent and D. Sinton, *Nature Synthesis*, 2023, **2**, 403–412.

60 M. Sun, J. Cheng and M. Yamauchi, *Nat. Commun.*, 2024, **15**, 1–9.

61 M. E. Leonard, M. J. Orella, N. Aiello, Y. Román-Leshkov, A. Forner-Cuenca and F. R. Brushett, *J. Electrochem. Soc.*, 2020, **167**, 124521.